Research Square

Preprints are preliminary reports that have not undergone peer review.
They should not be considered conclusive, used to inform clinical practice,
or referenced by the media as validated information.

Conservative phase-field modeling of fully Eulerian fluid--structure interaction

Nil Trujillo
Universitat Politècnica de Catalunya
Antonio Brunaccini
Universitat Politècnica de Catalunya
Seyyed Mahmoud Mousavi
Universitat Politècnica de Catalunya
Francesco Capuano
francesco.capuano@upc.edu
Universitat Politècnica de Catalunya

Research Article

Keywords: Fluid–structure interaction, fully Eulerian method, conservative phase field, diffuse interface, hyperelastic deformation, interface resolution

Posted Date: November 17th, 2026

DOI: https://doi.org/10.21203/rs.3.rs-11614587/v1

License: This work is licensed under a Creative Commons Attribution 4.0 International License.
Read Full License

Additional Declarations: No competing interests reported.

Conservative phase-field modeling of fully Eulerian fluid–structure interaction

Nil Trujillo[1], Antonio Brunaccini[1], Seyyed Mahmoud Mousavi[1], Francesco Capuano[1*]

[1*]Department of Fluid Mechanics, Universitat Politècnica de Catalunya · BarcelonaTech (UPC), Barcelona, 08019, Spain.

*Corresponding author(s). E-mail(s): francesco.capuano@upc.edu;
Contributing authors: ; ; ;

Abstract

We present a fully Eulerian, one-domain method for fluid–structure interaction (FSI) between incompressible fluids and hyperelastic solids, in which the solid indicator is transported by a conservative phase-field equation of Allen–Cahn type. Solid deformation is described by an Eulerian left Cauchy–Green tensor whose phase-weighted elastic stress enters a single momentum balance. Because the interface transport is written in flux form on a staggered Cartesian grid, the phase integral is conserved to machine precision and different regularization strategies can be exchanged without modifying the mechanical solver. The method thus adds conservative phase-field transport to the volume-of-fluid, level-set, reference-map and Cahn–Hilliard formulations available for fully Eulerian FSI. We instantiate it with three regularizations (CDI, ACDI and UWCDI) and assess them on two benchmarks. For a deformable disk in a lid-driven cavity, all variants reproduce the reference centroid path under grid refinement while differing in contour regularity and effective interface width. For a wall-supported filament under Kolmogorov forcing, severe bending creates narrow connections whose discrete topology depends on the regularization and, for CDI, strongly on resolution. Global observables are therefore robust to the choice of interface flux, whereas the geometry and connectivity of near-grid-scale features are not, with direct implications for FSI in strongly forced and turbulent flows.

Keywords: Fluid–structure interaction, fully Eulerian method, conservative phase field, diffuse interface, hyperelastic deformation, interface resolution

1 Introduction

Deformable solids interacting with strong or turbulent flows are ubiquitous in engineering and biology. Compliant coatings modify near-wall turbulence and skin friction (Rosti and Brandt 2017), while bacterial biofilms exposed to flow develop slender filamentous streamers that oscillate, thin and eventually detach (Rusconi et al. 2010; Drescher et al. 2013; Tierra et al. 2015). These problems combine large, history-dependent solid deformation with the formation of thin structural features, and both aspects are difficult to capture with interface-fitted methods. Arbitrary Lagrangian–Eulerian (ALE) formulations represent the interface sharply (Hu et al. 2001), but large deformations require repeated mesh motion or remeshing. Immersed methods (Mittal and Iaccarino 2005; Griffith and Patankar 2020) avoid this by solving the flow on a fixed grid, while still describing the solid on a separate Lagrangian discretization.

Fully Eulerian methods go one step further and describe both the fluid and the solid on the same fixed grid. Existing formulations can be organized along two largely independent choices. The first is how solid kinematics are represented in the Eulerian frame: by transporting the left Cauchy–Green tensor or the deformation gradient (Sugiyama et al. 2011; Ii et al. 2011; Takagi et al. 2012), by the reference map (Valkov et al. 2015; Rycroft et al. 2020; Jain et al. 2019), by an initial-point-set function within a monolithic variational setting (Dunne 2006; Richter 2013; Wick 2013), or by level-set-based elasticity (Cottet et al. 2008). The second is how the material indicator is transported: options include volume-of-fluid functions (Sugiyama et al. 2011; Ii et al. 2012; Rosti and Brandt 2017), level sets (Cottet et al. 2008; Valkov et al. 2015; Rycroft et al. 2020; Jain et al. 2019), or phase fields, either of Cahn–Hilliard type (Mokbel et al. 2018) or of Allen–Cahn type within stabilized finite-element frameworks (Sun et al. 2014; Mao and Jaiman 2023). In one-domain (one-continuum) formulations the indicator has a dual role: it defines the represented solid geometry and, through phase weighting, the spatial support of the elastic stress in the momentum balance. Its transport therefore influences not only geometric fidelity but also the mechanical coupling itself, and this influence grows as deforming structures develop features comparable to the grid spacing (Jemison et al. 2015).

In two-phase flows, a family of conservative Allen–Cahn models has recently emerged as an attractive compromise between the geometric accuracy of sharp-interface methods and the simplicity of diffuse-interface ones (Mirjalili et al. 2017). Building on the conservative level set of Olsson and Kreiss (2005), the conservative diffuse-interface (CDI) method of Chiu and Lin (2011) transports the phase field in conservative form and maintains a finite transition layer through a balance between diffusion and interface-normal compression. The boundedness of a centred CDI discretization was established by Mirjalili et al. (2020); the accurate conservative diffuse-interface (ACDI) method of Jain (2022) evaluates the regularization fluxes through an auxiliary signed-distance-like variable to allow sharper interfaces; and the upwind conservative diffuse-interface (UWCDI) method of Pirozzoli et al. (2025) replaces explicit diffusion with the numerical diffusion of upwind transport. These models are second order in space, local, explicit, and discretely conservative, which makes them well suited to large-scale simulations of turbulent multiphase flows on structured grids. Yet, to our knowledge, they have not been combined with Eulerian

hyperelasticity in a one-domain FSI framework. Existing Allen–Cahn FSI formulations rely on variational finite-element discretizations with additional conservation and geometry-preserving mechanisms (Mao and Jaiman 2023), whereas Cahn–Hilliard formulations involve a fourth-order operator (Mokbel et al. 2018).

In this work, we develop a conservative phase-field, one-domain method for incompressible fluid–hyperelastic solid interaction, and we use it to assess how the choice of conservative interface flux propagates into the coupled mechanical response. The method combines (i) a phase-weighted neo-Hookean stress built from an Eulerian left Cauchy–Green tensor, (ii) a phase-dependent logarithmic relaxation that drives the structural tensor to the identity in the fluid without altering the solid, and (iii) a flux-form phase-field transport on a staggered marker-and-cell grid, in which the regularization flux is a modular component. Keeping the mechanical formulation, structural-tensor transport and time integration fixed, we instantiate the framework with CDI, ACDI and UWCDI. Two benchmarks probe complementary aspects of the coupling: a deformable disk in a lid-driven cavity (Sugiyama et al. 2011), which tests global solid motion against a reference solution, and a wall-supported filament under Kolmogorov forcing, which drives severe bending and the formation of narrow connections. The results show that phase conservation and global motion are robust to the choice of regularization, whereas local geometry and discrete connectivity of near-grid-scale features are not.

The paper is organized as follows. Section 2 introduces the one-domain FSI formulation, and Section 3 the three conservative phase-field models. Section 4 describes the common numerical framework and the diagnostics. Section 5 presents the two benchmarks, and Section 6 summarizes the conclusions.

2 Mathematical formulation

2.1 Fully Eulerian one-domain FSI formulation

We consider an incompressible fluid interacting with a hyperelastic solid in a fixed domain $\Omega \subset \mathbb{R}^2$. Rather than tracking the moving boundary explicitly, we describe both phases using a common Eulerian velocity $\mathbf{u}(\mathbf{x}, t)$ and pressure $p(\mathbf{x}, t)$, and represent their spatial distribution with the phase indicator $\phi(\mathbf{x}, t)$. This indicator is approximately zero in the fluid and one in the solid, so its transition layer captures the evolving interface on the fixed grid.

The two phases have equal, constant densities and share the same viscosity coefficient. Removing these contrasts allows us to focus on how the phase-field discretization affects the coupled mechanical response. The constitutive responses nevertheless differ: the fluid is purely viscous, while the solid also supports hyperelastic stress. With the common density normalized to unity, the nondimensional governing equations are

$$\nabla \cdot \mathbf{u} = 0, \tag{1}$$

$$\frac{\partial \mathbf{u}}{\partial t} + \mathbf{u} \cdot \nabla \mathbf{u} = -\nabla p + \nabla \cdot (2\nu \mathbf{D}) + \nabla \cdot (\phi \boldsymbol{\tau}_s) + \mathbf{f}_{\text{ext}}, \tag{2}$$

where $\mathbf{D} = (\nabla \mathbf{u} + \nabla \mathbf{u}^T)/2$ is the rate-of-deformation tensor, ν is the common nondimensional kinematic viscosity, and $\mathbf{f}_{\text{ext}}$ is an imposed body force. The elastic extra

stress $\boldsymbol{\tau}_s$ enters the momentum equation weighted by ϕ, confining its contribution to the solid and its diffuse interfacial region. For each result, the Reynolds number is defined from its characteristic velocity and length scales as $Re = U_{\mathrm{ref}} L_{\mathrm{ref}}/\nu$.

2.2 Eulerian structural tensor and elastic response

We describe the solid's deformation in the Eulerian frame using the symmetric structural field $\boldsymbol{\sigma}$. For an initially undeformed, incompressible solid, this field corresponds to the left Cauchy–Green tensor,

$$\boldsymbol{\sigma} = \mathbf{F}\mathbf{F}^T, \tag{3}$$

where $\mathbf{F}$ is the deformation gradient. Related Eulerian formulations have been used in diffuse-interface FSI (Mokbel et al. 2018). From $\boldsymbol{\sigma}$, we define the solid's elastic extra stress as

$$\boldsymbol{\tau}_s = \mathcal{G}\left(\boldsymbol{\sigma} - \mathbf{I}\right), \tag{4}$$

where $\mathcal{G}$ is the shear-modulus coefficient in the solver's stress normalization and $\mathbf{I}$ is the identity. Within the solid, the structural field evolves kinematically with the flow according to

$$\frac{\partial \boldsymbol{\sigma}}{\partial t} + \mathbf{u}\cdot\nabla\boldsymbol{\sigma} = (\nabla\mathbf{u})\boldsymbol{\sigma} + \boldsymbol{\sigma}(\nabla\mathbf{u})^T. \tag{5}$$

Starting from $\boldsymbol{\sigma} = \mathbf{I}$, the continuous incompressible evolution preserves positive definiteness and unit determinant:

$$\det\boldsymbol{\sigma} = 1. \tag{6}$$

We use these properties as consistency diagnostics, although the discrete transport does not enforce them exactly. Because the field is stored throughout the fixed Eulerian domain, a common phase-dependent numerical extension is applied outside the solid core; its definition and implementation are given in Sect. 4.

2.3 Diffuse-interface representation and coupling

The phase field links the interface geometry to the mechanical response. We represent the fluid–solid boundary by the $\phi = 1/2$ contour, while the local phase-field value weights the structural stress in Eq. (2), distributing the elastic forcing across the diffuse layer. Changes in the transported profile can therefore alter both the represented shape and the elastic loading. This altered loading affects the velocity and solid deformation, which in turn feed back into subsequent phase transport. Interface resolution thus influences not only geometric fidelity but also the mechanical coupling across the diffuse interface.

The following sections describe the conservative phase-field formulations (Sect. 3) and their spatial discretizations (Sect. 4.3), which determine how this coupling is represented numerically.

3 Conservative phase-field formulations

To evolve the material indicator in this fully Eulerian framework, we use three conservative phase-field formulations from the Allen–Cahn family: the conservative

diffuse-interface (CDI), the accurate conservative diffuse-interface (ACDI), and the upwind conservative diffuse-interface (UWCDI) methods.

While all three conserve ϕ, they maintain its transition layer through different balances: CDI and ACDI balance explicit diffusive spreading against compression, whereas UWCDI uses compression to counteract numerical diffusion introduced by upwind transport. ACDI also uses an auxiliary variable to evaluate the interface normal and compressive flux. The regularization strategy therefore determines the profile realized on the grid and, in turn, how well thin or strongly deformed structures remain resolved.

3.1 Conservative diffuse-interface method (CDI)

Introduced by Chiu and Lin (2011), CDI transports the phase indicator conservatively and maintains its diffuse transition through a balance of diffusive and compressive fluxes:

$$\frac{\partial \phi}{\partial t} + \nabla \cdot (\phi \mathbf{u}) = \nabla \cdot \left[D_\Gamma \nabla \phi - C_\Gamma \phi (1-\phi) \mathbf{n}_\phi \right], \tag{7}$$

where

$$\mathbf{n}_\phi = \frac{\nabla \phi}{\sqrt{|\nabla \phi|^2 + \delta_n^2}}, \qquad D_\Gamma = \frac{C_\Gamma \varepsilon}{2}. \tag{8}$$

Here, ε controls the characteristic interface thickness, C_Γ sets the regularization rate, and δ_n prevents singularities when evaluating the interface normal. Diffusion smooths the phase-field profile, while compression counters this spreading. Their balance determines the equilibrium profile.

3.2 Accurate conservative diffuse-interface method (ACDI)

ACDI, introduced by Jain (2022), builds on the same diffusion–compression balance but uses an auxiliary signed-distance-like variable to evaluate the interface normal and compressive flux:

$$\psi = \varepsilon_A \ln \left(\frac{\widehat{\phi} + \delta_\psi}{1 - \widehat{\phi} + \delta_\psi} \right), \tag{9}$$

where $\widehat{\phi} = \min(1, \max(0, \phi))$ is used only in the auxiliary logarithm and $\delta_\psi = 10^{-100}$ prevents singularities. Thus, clipping regularizes the evaluation of ψ without modifying the transported phase field. The phase field then evolves according to

$$\frac{\partial \phi}{\partial t} + \nabla \cdot (\phi \mathbf{u}) = \nabla \cdot \left\{ \Gamma \left[\varepsilon_A \nabla \phi - \frac{1}{4} \left(1 - \tanh^2 \left(\frac{\psi}{2\varepsilon_A} \right) \right) \mathbf{n}_\psi \right] \right\}, \tag{10}$$

with

$$\mathbf{n}_\psi = \frac{\nabla \psi}{\sqrt{|\nabla \psi|^2 + \delta_n^2}}. \tag{11}$$

Here, ε_A controls the interface thickness and Γ determines the regularization rate. Unlike CDI, ACDI reconstructs the interface normal and compressive contribution

from ψ, while retaining ϕ in the diffusive term. The normal regularization is $\delta_n = 10^{-6}$ for CDI and 10^{-14} for ACDI and UWCDI.

For a stationary planar interface, diffusion and compression balance, giving the ideal equilibrium profiles:

$$\begin{aligned} \phi_{\mathrm{eq}}^{\mathrm{CDI}}(d) &= \frac{1}{2}\left[1 - \tanh\left(\frac{d}{\varepsilon}\right)\right], \\ \phi_{\mathrm{eq}}^{\mathrm{ACDI}}(d) &= \frac{1}{2}\left[1 - \tanh\left(\frac{d}{2\varepsilon_A}\right)\right], \end{aligned} \tag{12}$$

where d is the signed distance from the interface, positive toward the fluid. These profiles coincide when the thickness parameters satisfy

$$\varepsilon = 2\varepsilon_A. \tag{13}$$

This relation matches the continuous equilibrium profiles; it does not imply identical interface widths in the discrete implementations.

3.3 Upwind conservative diffuse-interface method (UWCDI)

UWCDI, introduced by Pirozzoli et al. (2025), takes a different route: it removes explicit diffusion and uses the numerical diffusion of upwind transport as a spreading mechanism counteracted by compression,

$$\frac{\partial \phi}{\partial t} + \nabla \cdot [\phi \mathbf{u} + \beta \phi(1-\phi)\mathbf{n}_\phi] = 0. \tag{14}$$

In our simulations, UWCDI starts from a sharp cell-centered indicator: $\phi = 1$ inside the solid and $\phi = 0$ outside. Upwind transport generates intermediate values as the interface moves, while the compressive flux counters their spreading. The transition layer thus emerges dynamically from the spatial discretization, without an explicit diffusion term or a separate reinitialization procedure.

Equations (7)–(14) describe the continuous transport laws; the realized interface profiles also depend on how their fluxes are discretized. The next section describes the common numerical framework used to implement these laws and couple them to the fluid and structural equations.

4 Numerical framework

The formulations described above are implemented within a shared fully Eulerian FSI solver. We keep the elastic law, momentum discretization, structural-field transport, projection procedure, and time-integration scheme fixed across all cases. The method-dependent components are the phase-field transport laws and their spatial discretizations, described below.

4.1 Common spatial and temporal discretization

We discretize the domain on a Cartesian marker-and-cell (MAC) grid (Harlow and Welch 1965). Velocity components lie at cell faces, while pressure, ϕ, and the independent components of $\boldsymbol{\sigma}$ are cell-centered. Momentum convection uses a conservative staggered finite-difference operator based on centered face and corner products; pressure gradients and viscous terms use centered differences.

We advance all cases with the CN/RKW3 IMEX scheme, using the four-stage tableau reported in Eq. (23) of Cavaglieri and Bewley (2015). Viscous terms are treated implicitly, while convection, elastic forcing, phase transport, and structural-field evolution are explicit. At the start of each time step, we verify that the velocity carried over from the preceding step is divergence-compatible. We then follow each velocity predictor with a fractional-step projection (Perot 1993). Although the IMEX tableau is second-order accurate, this does not imply global second-order accuracy for the complete projected FSI algorithm. The time-step policy is also common to all formulations.

4.2 Structural transport and numerical extension

We discretize the advection of $\boldsymbol{\sigma}$ conservatively with first-order upwinding and evaluate the deformation terms in Eq. (5) using centered velocity gradients. This upwind treatment was selected because less dissipative schemes led to a loss of positive definiteness during solver development; it does not, however, enforce $\det \boldsymbol{\sigma} = 1$ exactly. The velocity projection controls discrete divergence but does not by itself impose this constraint on the transported structural tensor.

We store $\boldsymbol{\sigma}$ throughout the Eulerian domain, even though it contributes mechanically only within the solid. To suppress spurious deformation history in the surrounding fluid, we add a phase-dependent numerical extension to the right-hand side of its evolution equation:

$$\mathcal{R}_{\text{ext}} = -\kappa(\phi)\boldsymbol{\sigma} \log \boldsymbol{\sigma}, \qquad \kappa(\phi) = \kappa_0(1-\phi)^m, \tag{15}$$

where $\log \boldsymbol{\sigma}$ denotes the matrix logarithm of the symmetric positive-definite field. The extension vanishes in the solid limit ($\phi = 1$) and drives $\boldsymbol{\sigma}$ toward the identity in the fluid. It is purely numerical and does not represent physical stress relaxation. We take $\kappa_0 = 20$, $m = 4$, and reset $\boldsymbol{\sigma} = \mathbf{I}$ only for $\phi < 10^{-6}$. The law and parameters are the same in both benchmarks and for all phase-field formulations. Because κ depends on the evolving ϕ, the extension remains active within diffuse transition regions where elastic stress still contributes to momentum. Its spatial action therefore follows the evolving interface profile.

4.3 Spatial discretization of the interface flux

At the discrete level, each formulation evolves the cell-centered phase indicator through the divergence of a face flux $\mathbf{F}_\phi$. The shared semi-discrete form is

$$\frac{d\phi_i}{dt} = -\left(\nabla_h \cdot \mathbf{F}_\phi\right)_i . \tag{16}$$

The flux definitions below encode each method's advection and regularization strategy.

For CDI, the flux at a face f normal to coordinate direction j is

$$F^{\mathrm{CDI}}_{\phi,j,f} = u_{j,f}\phi^{\mathrm{up}}_f + C_\Gamma \left[\overline{\phi(1-\phi)n_{\phi,j}}_f - \frac{\varepsilon}{2}(\partial_j\phi)_f\right]. \tag{17}$$

We select the advected value ϕ^{up}_f by first-order upwinding according to the sign of the face velocity. Centered differences provide the diffusive gradient at the face, while the cell-centered sharpening vector is interpolated there.

This implementation retains the original CDI mathematical formulation of Chiu and Lin (2011), while employing a spatial discretization adapted to the present staggered-grid FSI solver. In particular, it differs from both the spatial scheme of the original work and the centered discretization analyzed by Mirjalili et al. (2020). Boundedness guarantees reported for that centered scheme cannot be assumed to hold for this implementation.

ACDI uses centered interpolation for material advection, giving the following face flux:

$$\begin{aligned} F^{\mathrm{ACDI}}_{\phi,j,f} &= u_{j,f}\overline{\phi}_f \\ &\quad + \Gamma\left[\frac{1}{4}\left(1-\tanh^2\left(\frac{\overline{\psi}_f}{2\varepsilon_A}\right)\right)\overline{n}_{\psi,j,f} - \varepsilon_A(\partial_j\phi)_f\right]. \end{aligned} \tag{18}$$

We evaluate ψ and its normalized gradient at cell centers, then interpolate them to faces. The diffusive gradient of ϕ is computed there using centered differences. This combination of centered advection and diffusion with auxiliary-variable sharpening follows the spatial formulation of Jain (2022). The values of Γ used in each case are listed with the numerical parameters.

In UWCDI, material advection and interface compression share a single upwind face flux:

$$F^{\mathrm{UWCDI}}_{\phi,j,f} = \phi^{\mathrm{up}}_f\left[u_{j,f} + \beta_{j,f}n_{\phi,j,f}\left(1-\phi^{\mathrm{up}}_f\right)\right], \tag{19}$$

where

$$\beta_{j,f} = \frac{|u_{j,f}|}{\alpha_{j,f}}. \tag{20}$$

We reconstruct the interface normal from centered phase-field gradients, interpolate it to faces, and renormalize it there. The parameter $\alpha_{j,f}$ controls the effective interface thickness and incorporates a grid-aspect correction when the mesh spacing differs between coordinate directions. No explicit diffusive flux is introduced: the compression is balanced by the numerical diffusion of the upwind operator, following the spatial strategy of (Pirozzoli et al. 2025).

Table 1 Method-dependent components of the phase-field spatial discretization. All remaining components of the FSI solver are identical across the three formulations.

	CDI	ACDI	UWCDI
Advection	Upwind	Centered	Upwind
Interface normal	$\nabla\phi$	$\nabla\psi$	$\nabla\phi$
Explicit diffusion	Yes	Yes	No
Compression	CDI flux	Auxiliary-variable flux	Upwind flux
Main parameters	C_Γ, ε	Γ, ε_A	α

The original multidimensional UWCDI formulation uses directional Strang splitting. Here, we retain its spatial flux but advance it with the common IMEX scheme used for CDI and ACDI. We therefore do not assume that fully discrete boundedness or monotonicity properties associated with the original splitting carry over to this solver.

Table 1 summarizes the method-dependent components of each spatial flux. Because advection and regularization vary together, each formulation is treated as a complete discretization rather than as an isolated change to one flux component.

At impermeable non-periodic walls, the normal CDI/ACDI regularization flux is set to zero. For UWCDI, the normal face flux also vanishes under no penetration, since both its advective and compressive contributions scale with the normal face velocity. Prescribed wall values of ϕ are used in boundary reconstructions and do not introduce a net phase flux.

4.4 Diagnostics

We first monitor conservation through the phase integral and its relative change:

$$M_\phi(t) = \int_\Omega \phi(\mathbf{x}, t)\, \mathrm{d}\Omega, \qquad E_M(t) = \frac{M_\phi(t) - M_\phi(0)}{M_\phi(0)}, \tag{21}$$

We characterize the global thickness of the transition layer using the integral measure

$$w_{\mathrm{eff}}(t) = \frac{\displaystyle\int_\Omega 4\widehat{\phi}(1-\widehat{\phi})\, \mathrm{d}\Omega}{\displaystyle\int_\Omega |\nabla\phi|\, \mathrm{d}\Omega}. \tag{22}$$

Only the numerator uses clipped values; the denominator uses the gradient of the unmodified phase indicator. In the discrete measure, we reconstruct cell-centered gradients from staggered face differences. For the ideal planar profiles in Eq. (12), this definition gives $w_{\mathrm{eff}} = 2\varepsilon$ for CDI and $w_{\mathrm{eff}} = 4\varepsilon_A$ for ACDI. UWCDI has no prescribed continuous equilibrium width: its transition thickness emerges from the discrete balance between upwind numerical diffusion and compression. Consequently, the sharp initial condition has $w_{\mathrm{eff}}(0) = 0$, and a finite width develops only as the interface is

transported. As a domain-integrated measure, w_{eff} does not reveal local thinning or broadening around features such as narrow necks.

To track the body's global motion, we compute its phase-weighted centroid:

$$\mathbf{x}_c(t) = \frac{1}{M_\phi(t)} \int_\Omega \mathbf{x}\phi(\mathbf{x}, t)\, \mathrm{d}\Omega. \tag{23}$$

Within the solid core $\Omega_{\text{core}}(t) = \{\mathbf{x} : \phi \geq 0.9\}$, we assess consistency with incompressible deformation using

$$E_{\text{det}}^{\text{core}}(t) = \frac{\displaystyle\int_{\Omega_{\text{core}}} |\det \boldsymbol{\sigma} - 1|\, \mathrm{d}\Omega}{\displaystyle\int_{\Omega_{\text{core}}} \mathrm{d}\Omega}, \tag{24}$$

We also record the minimum eigenvalue of $\boldsymbol{\sigma}$ and the number of core cells that are not positive definite.

In the wall-supported filament benchmark (Sect. 5.2), the solid domain also contains a supporting layer. To separate its contribution from that of the deformable structure, we evaluate the determinant error over the region above the support as well:

$$\Omega_{\text{core}}^{\text{upper}}(t) = \{(x, y) : \phi(x, y, t) \geq 0.9, \quad y > h_b\}, \tag{25}$$

Here, h_b is the supporting-layer height specified in Sect. 5.2. We compute the corresponding mean error, $E_{\text{det}}^{\text{upper}}$, with the same area-normalized definition as in Eq. (24). This restriction removes most of the support from the average, but, being defined in Eulerian space, does not track a fixed set of material points.

Together, these diagnostics track phase conservation, global motion, and deformation consistency, complementing the interface geometries examined in the following results.

5 Numerical results and discussion

The two cases address complementary aspects of the coupled response: the deformation of a solid inclusion in a lid-driven cavity and the evolution of a slender, wall-supported structure under spatially alternating forcing.

5.1 Deformable disk in a lid-driven cavity

Configuration and reference.

We first consider the deformable-disk case of Sugiyama et al. (2011). A circular solid of radius $R_0 = 0.2$ is centered at $(0.6, 0.5)$ in a unit-square cavity whose top lid moves at $U_{\text{lid}} = 1$. The phases have equal density $\rho = 1$ and share the viscosity coefficient $\nu = 0.01$; with $\mathcal{G} = 0.1$, these parameters give $Re = 100$. The remaining walls are stationary and no-slip, while ϕ and the structural-field components satisfy

Table 2 Configuration of the lid-driven-cavity benchmark. Interface parameters are scaled with the grid spacing $h = 1/N$.

Category	Parameter	Value / setting
Physical	Domain	$\Omega = [0,1]^2$
	Initial disk center	$(x_{c,0}, y_{c,0}) = (0.6, 0.5)$
	Initial radius	$R_0 = 0.2$
	Lid velocity	$U_{\text{lid}} = 1$
	Density	$\rho_f = \rho_s = 1$
	Common viscosity coefficient	$\nu = 0.01$
	Elastic shear modulus	$\mathcal{G} = 0.1$
Numerical	Reynolds number	$Re = 100$
	Grid resolution	$N = 64,\ 128,\ 256$
	Final time	$T = 20$
	Hyperbolic CFL limit	0.1
	Interface CFL limits	0.25 (compression), 0.5 (diffusion)
	Maximum time step	$\Delta t_{\max} = 5 \times 10^{-3}$
CDI	Initial profile	Hyperbolic tangent
	Interface thickness	$\varepsilon/h = 2$
	Regularization	$C_\Gamma = 4$
ACDI	Initial profile	Hyperbolic tangent
	Interface thickness	$\varepsilon_A/h = 0.51$
	Regularization	$\Gamma = 1$
UWCDI	Initial profile	Sharp indicator
	Compression parameter	$\alpha = 1$
	Normal reconstruction	Standard phase-gradient normal

homogeneous Neumann conditions. We consider grid resolutions $N = 64, 128, 256$; the other numerical settings are listed in Table 2.

CDI and ACDI use their respective hyperbolic-tangent initial profiles, whereas UWCDI starts from a sharp cell-centered indicator, consistent with the discontinuous-interface tests of Pirozzoli et al. (2025). The digitized centroid trajectory of Sugiyama et al. (2011) provides an independent reference for one global FSI observable, the centroid-path geometry, but not for the interface discretizations.

Global response and interface geometry.

The centroid trajectories in Fig. 1 show broad geometric agreement with the digitized reference, especially at the two finest resolutions. Because the reference contains spatial coordinates but no time labels, the comparison assesses path geometry rather than time-resolved agreement. The largest discrepancy occurs for CDI at $N = 64$, particularly after the first orbit, whereas the ACDI and UWCDI trajectories are close at the two finest resolutions.

All nine simulations conserve M_ϕ to within a maximum relative error of 1.6×10^{-12}, with excursions outside $[0, 1]$ below 5×10^{-14}. Conservation of the initial phase integral, however, does not imply agreement with the geometrical disk area. To quantify this

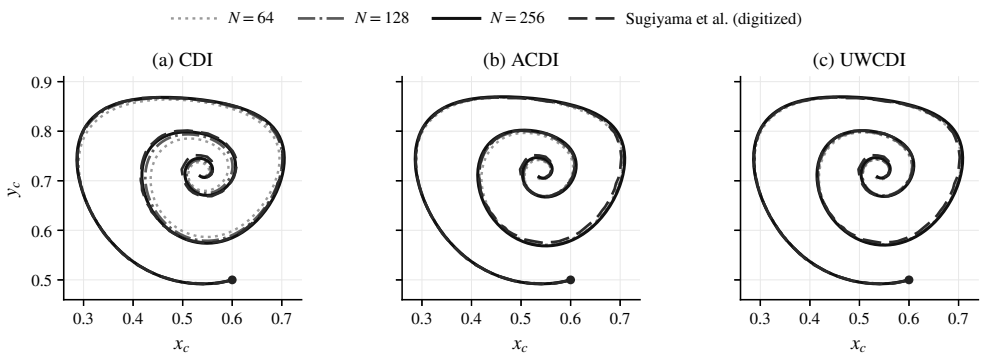


Fig. 1 Phase-weighted centroid trajectories in the lid-driven cavity: (a) CDI, (b) ACDI and (c) UWCDI for $N = 64, 128, 256$. The digitized result of (Sugiyama et al. 2011) is shown as a reference. The initial position is $(0.6, 0.5)$.

Table 3 Initial phase-area bias and effective interface thickness in the lid-driven-cavity benchmark. The interface thickness is expressed in grid cells.

N	Method	$E_A(0)$ (%)	$w_{\mathrm{eff}}(0)/h$	$w_{\mathrm{eff}}(20)/h$
64	CDI	+2.008	4.003	4.053
	ACDI	+0.522	2.040	2.023
	UWCDI	−0.140	0.000	2.009
128	CDI	+0.502	4.000	4.044
	ACDI	+0.131	2.039	2.017
	UWCDI	+0.055	0.000	2.008
256	CDI	+0.125	4.000	4.044
	ACDI	+0.033	2.038	2.017
	UWCDI	+0.030	0.000	2.003

initialization bias, we define

$$E_A(0) = \frac{M_\phi(0) - \pi R_0^2}{\pi R_0^2}. \tag{26}$$

Table 3 reports this bias alongside the effective interface thickness at initialization and at $T = 20$.

The area bias decreases under refinement. At $T = 20$, however, the effective interface thickness remains method dependent in grid units: it is approximately $4h$ for CDI and $2h$ for ACDI, while UWCDI develops a transition of about $2h$ from its initially sharp indicator.

The shapes in Fig. 2 show similar large-scale deformation, despite local differences in interface geometry. ACDI maintains a comparatively regular contour, whereas UWCDI develops localized corrugations during strong deformation. A targeted sensitivity test at $N = 128$ shows that a Youngs-type normal attenuates the strongest

corrugations; the nine-point-smoothed normal gives a similar contour, while diffuse initialization modifies it only modestly. These variants have little effect on the centroid trajectory or phase conservation (Appendix A). All baseline UWCDI runs use the same centered-difference normal reconstruction.

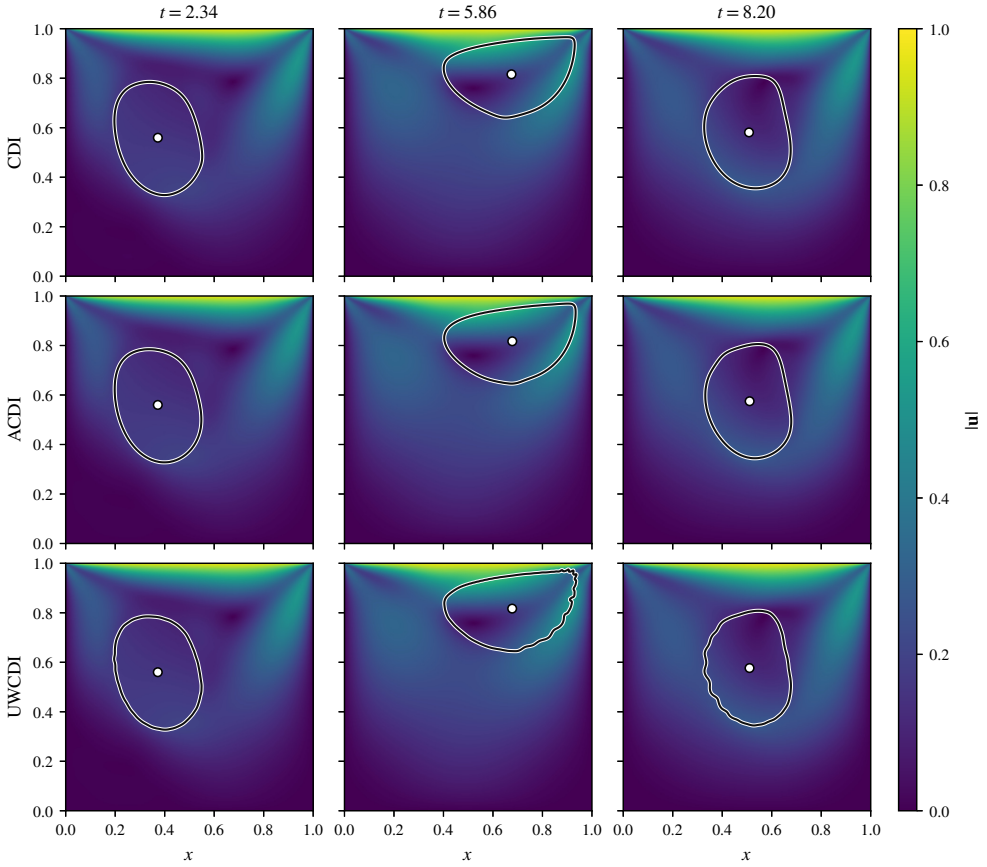


Fig. 2 Deformation of the inclusion at $N = 256$ for CDI, ACDI, and UWCDI (rows), at $t = 2.34$, 5.86, and 8.20 (columns). The background indicates velocity magnitude; the overlaid contour corresponds to $\phi = 0.5$ and the marker identifies the phase-weighted centroid. All panels use the same velocity scale.

Structural-tensor consistency.

At $T = 20$, the solid-core determinant error decreases with refinement for all three methods. For $N = 64, 128, 256$, it is $(0.344, 0.238, 0.155)$ for CDI, $(0.336, 0.239, 0.157)$ for ACDI, and $(0.333, 0.242, 0.165)$ for UWCDI. Despite this decrease, the errors remain appreciable, although none of the nine simulations produces a non-positive-definite structural tensor in the solid core. The similar error magnitudes are consistent with a contribution from the common structural-field transport, but do not distinguish

it from effects of the phase-dependent extension or differences in deformation history. The centroid-path agreement above provides an independent check of one global response, but does not establish that these determinant deviations are mechanically negligible or that the full deformation field is reproduced.

5.2 Wall-supported filament under Kolmogorov forcing

Test-case configuration.

We use an idealized wall-supported hyperelastic filament as a numerical test of phase-field transport under strong deformation. Wall-mounted flexible structures have been studied under oscillatory flow (Zhao et al. 2008; Kanchan and Maniyeri 2020), and related slender structures occur in systems such as biofilm streamers (Tierra et al. 2015). Here, the prescribed forcing drives large bending and generates narrow connections, allowing us to examine how the phase-field methods represent connectivity as these features become difficult to resolve. Accordingly, loss of connectivity in the thresholded phase field is a numerical outcome, not a prediction of physical fracture. All reported times are nondimensional simulation times for this prescribed configuration, not physical rupture times.

The computational domain is $\Omega = [0, 6] \times [0, 2]$, with periodic boundary conditions in x and no-slip walls in y. A solid layer of height $h_b = 0.2$ supports a vertical filament centered at $x_0 = 3$, with width $W = 0.30$ and unsupported height $H_f = 1$. Its upper end is rounded with a semicircular cap of radius $R = 0.15$. Both the filament and its support belong to the same solid phase, so no additional interface condition is imposed at their junction.

The flow is driven by a steady, spatially alternating Kolmogorov body force,

$$\mathbf{f}_{\text{ext}}(y) = \big(A_K \sin(k_y y), 0\big), \qquad k_y = \frac{2\pi n}{L_y}, \qquad A_K = \nu k_y^2 U_{\text{ref}}. \tag{27}$$

With $n = 2$, $L_y = 2$, $U_{\text{ref}} = 0.5$, and $\nu = 0.01$, we obtain $A_K \simeq 0.197392$ and $Re_{\text{eff}} = U_{\text{ref}} H_f / \nu = 50$.

The fluid is initially at rest apart from a small, prescribed velocity perturbation introduced to seed streamwise variations. This perturbation is defined through the streamfunction

$$\Psi_p(x, y) = \frac{A_p}{k_x} \cos(k_x x) \sin^2\left(\frac{\pi y}{L_y}\right), \qquad k_x = \frac{2\pi m_x}{L_x}, \tag{28}$$

where $A_p = 0.02$ and $m_x = 1$. The initial velocity is

$$\mathbf{u}(x, y, 0) = \left(\frac{\partial \Psi_p}{\partial y}, -\frac{\partial \Psi_p}{\partial x}\right). \tag{29}$$

In the numerical implementation, Ψ_p is evaluated at the vertices of the staggered MAC grid, and the velocity components are obtained using compatible finite differences. This ensures discrete incompressibility and satisfies the prescribed velocity boundary conditions. The same initial perturbation is used for all three methods.

Table 4 Configuration of the wall-supported filament. The grid parameter N denotes the number of cells in the vertical direction, with $N_x = 3N$, such that $\Delta x = \Delta y = h$.

Parameter	Value
Domain and boundaries	$[0, 6] \times [0, 2]$, periodic x, no-slip y
Support height h_b	0.20
Filament height H_f / width W	1.00 / 0.30
Initial center / cap radius	$x_0 = 3.00$ / $R = 0.15$
ρ, ν, $\mathcal{G}$	1, 0.01, 0.20
Forcing n, U_{ref}	2, 0.50
Initial perturbation parameter A_p	0.02
Main grid / final time	$N_x \times N_y = 384 \times 128$, $T = 20$
CDI: ε/h, C_Γ	2, 4
ACDI: ε_A/h, Γ	0.51, 1
UWCDI: α, initialization	1, sharp indicator

The primary simulations use a 384×128 grid and run to the nondimensional final time $T = 20$. The remaining numerical parameters are listed in Table 4. The prescribed phase-field values at the lower and upper walls correspond to the solid and fluid states, respectively; structural-tensor inflow data, where required, are undeformed.

Deformation and discrete connectivity.

Figure 3 shows the initially upright filament bending into an S-shaped geometry under the opposing flow layers. The subsequent evolution of the represented connections depends on the discretization: the thresholded phase field loses connectivity by $t = 10$ for CDI and at $t = 16$ for ACDI, whereas UWCDI remains connected through $T = 20$.

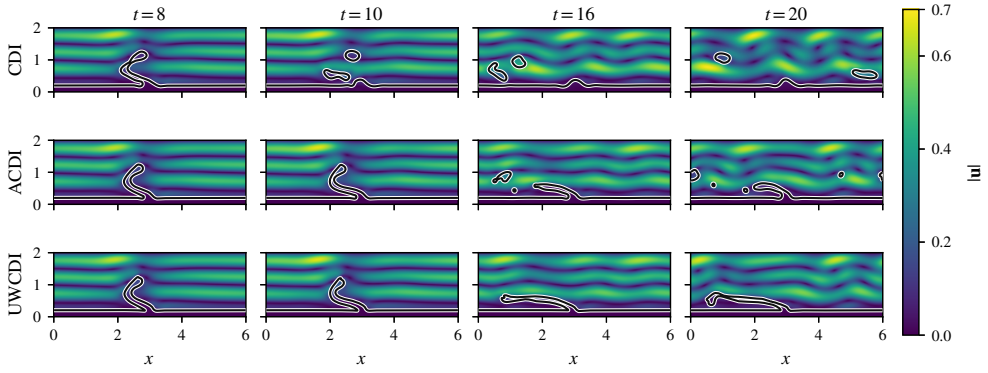


Fig. 3 Evolution of the wall-supported filament for $N_y = 128$: CDI, ACDI, and UWCDI (rows), shown at $t = 8, 10, 16, 20$ (columns). The background denotes velocity magnitude, and the superposed $\phi = 0.5$ contours identify the represented solid. A common velocity scale is used in all panels.

Table 5 Number of connected components of the thresholded region $\phi \geq 0.5$ on the 384×128 grid, accounting for periodic connectivity in x. These are discrete topological diagnostics, not physical fracture counts.

	$t = 8$	$t = 10$	$t = 12$	$t = 16$	$t = 20$
CDI	1	3	3	3	3
ACDI	1	1	1	3	5
UWCDI	1	1	1	1	1

The direction of the early bending can be understood from the undisturbed flow associated with Eq. (27),

$$u_{x,0}(y) = U_{\mathrm{ref}} \sin(2\pi y), \qquad u_{y,0} = 0. \tag{30}$$

Along the unsupported filament, this flow is rightward over $0.2 < y < 0.5$ and $1 < y < 1.2$, but leftward over $0.5 < y < 1$. The broad middle region contributes to the observed leftward bending.

To quantify this evolution, we count connected components of the thresholded cell-centered solid indicator,

$$\Omega_s^h(t) = \{\mathbf{x}_{ij} : \phi_{ij}(t) \geq 0.5\}, \tag{31}$$

using nearest-neighbor cell connectivity, including periodic links in x. Table 5 reports the resulting component counts: CDI has three components by $t = 10$, ACDI has five by $t = 20$, and UWCDI remains a single component throughout the simulated interval.

The phase integral is conserved to near machine precision in all three runs: the maximum relative errors are 1.50×10^{-13} (CDI), 2.58×10^{-14} (ACDI), and 1.86×10^{-13} (UWCDI). At $T = 20$, the domain-integrated effective widths are $4.020h$, $2.021h$, and $1.607h$, respectively. The initial phase-area biases are -0.031% (CDI), -0.0049% (ACDI), and $+1.93\%$ (UWCDI), so conservation within each run does not imply equal initial phase integrals across methods. The saved UWCDI fields show a small upper excursion of approximately 3×10^{-11} beyond $\phi = 1$. Its cause is not established, and the saved values do not establish boundedness at every intermediate integration stage.

The observed sequence is consistent with the effective interface thickness, relative to the width of narrow connections, influencing their discrete representation. However, the width reported here is a domain-integrated measure and does not quantify local neck thickness; the methods also differ in initialization and flux discretization. Moreover, because the elastic contribution enters the momentum equation through $\nabla \cdot (\phi \boldsymbol{\tau}_s)$, changes in ϕ alter the spatial distribution of elastic stress and feed back on the deformation. The connectivity differences therefore reflect the complete coupled numerical configurations and do not isolate interface thickness as the sole cause.

For ACDI, we use the fixed regularization parameter $\Gamma = 1$, which satisfies the criterion $\Gamma \geq |\mathbf{u}|_{\max}$ of Jain (2022) for the velocities reached in these simulations. Because Γ controls the strength of interface regularization, the evolution of narrow

connections may also depend on its value; we do not assess this parameter dependence here.

At $T = 20$, the full solid-core determinant errors are 0.0241 for CDI, 0.0531 for ACDI, and 0.0782 for UWCDI; the minimum tensor eigenvalue remains positive in every case. These averages include the supporting layer, which occupies most of the solid domain and has relatively small determinant errors. Restricting the diagnostic to the region above the support (Eq. (25)) raises the errors to 0.1543, 0.3072, and 0.4599, respectively. Thus, the full solid-core averages mask larger deviations from $\det \boldsymbol{\sigma} = 1$ in the deforming region. These values do not provide a direct ranking of the phase-field methods because the simulations follow different deformation histories, particularly after discrete connectivity is lost.

Illustration of grid-resolution sensitivity.

As a targeted illustration of resolution sensitivity for CDI, rather than a cross-method convergence study, we repeat the calculation on a coarser 192×64 grid with the same physical parameters and $\varepsilon/h = 2$. Thus, the ratio of regularization thickness to grid spacing is held fixed, while the filament's geometric features are represented by fewer cells. The two grids show similar early bending, but diverge as narrow connections form (Fig. 4).

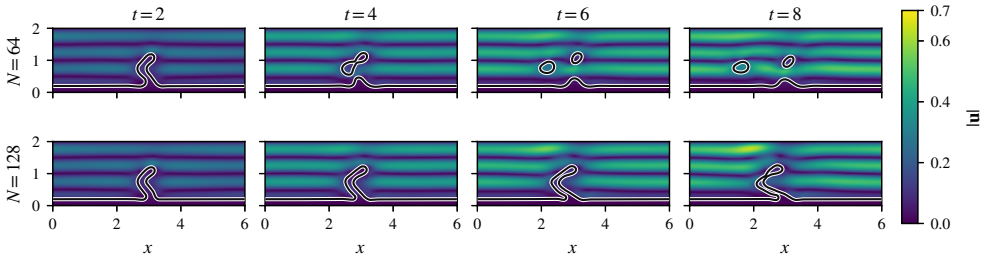


Fig. 4 Sensitivity of the CDI filament evolution to grid resolution, comparing $N_y = 64$ and $N_y = 128$ at $t = 2, 4, 6, 8$. Both runs use the same physical forcing and elastic response, while the coarser grid loses discrete connectivity earlier.

At $N_y = 64$, the thresholded phase region first loses connectivity between $t = 3$ and $t = 4$; at $N_y = 128$, this is first observed between saved fields at $t = 8$ and $t = 10$. This shift shows that the discrete connectivity transition is sensitive to spatial resolution; no mesh-converged transition time is established.

6 Conclusions

We have developed a fully Eulerian, one-domain FSI method in which a conservative, second-order Allen–Cahn equation transports the solid indicator, while an Eulerian left Cauchy–Green tensor provides the phase-weighted hyperelastic stress. The flux-form, staggered-grid formulation conserves the phase integral to machine precision and accommodates different regularization fluxes without changes to the mechanical solver; here it was instantiated with CDI, ACDI and UWCDI. Across both benchmarks, global observables proved robust to this choice, whereas local geometry and discrete

connectivity became strongly dependent on it once structural features approached the grid scale.

The two benchmarks illustrate this distinction. While the lid-driven cavity exhibits comparable global dynamics across the three implementations, the wall-supported filament reveals substantial differences in the persistence of narrow connections. These changes in connectivity are properties of the thresholded phase field, not predictions of physical fracture. The targeted CDI resolution test shows that this discrete transition can depend strongly on spatial resolution in the configuration studied. Moreover, because the methods differ in both their spatial fluxes and effective interface thicknesses, the present results do not establish which individual numerical mechanism is responsible for the observed differences.

These findings emphasize the importance of interface resolution when selecting a phase-field discretization for challenging FSI problems. Targeted sensitivity analyses could help disentangle the contributions of interface width, flux discretization, regularization, initialization, and grid resolution to the observed differences in local geometry and discrete connectivity, particularly as structural dimensions approach the grid scale.

An important extension of this work would be to repeat the comparison within an FSI framework that also accounts for solid growth. This would allow the influence of interface discretization to be examined when structural deformation is coupled to an evolving material geometry. Another priority is to improve the numerical transport of the structural tensor, particularly the preservation of its positive definiteness and the incompressibility constraint $\det \boldsymbol{\sigma} = 1$. Developing discretizations that better respect these properties would strengthen the reliability of fully Eulerian FSI simulations under large deformations.

A Sensitivity of the UWCDI interface geometry

In the lid-driven-cavity calculations, baseline UWCDI uses a sharp initial indicator and reconstructs its interface normal from second-order centered differences of ϕ at cell centers. We assess the sensitivity to these choices with auxiliary calculations at $N = 128$, varying the normal reconstruction and, in one case, the initial profile. The compression parameter $\alpha = 1$, momentum and structural-tensor discretizations, time integrator, and time-step policy are unchanged.

The first variant replaces the centered-gradient normal with a multidirectional Youngs-type reconstruction (Youngs 1982; Tryggvason et al. 2011), while retaining the sharp initialization. On a uniform Cartesian grid, the phase-field gradient is evaluated using the weighted 3×3 stencil

$$(\partial_x \phi)^Y_{i,j} = \frac{\phi_{i+1,j-1} + 2\phi_{i+1,j} + \phi_{i+1,j+1} - \phi_{i-1,j-1} - 2\phi_{i-1,j} - \phi_{i-1,j+1}}{8h}, \tag{32}$$

with the analogous expression in the y direction. The resulting gradient is normalized at cell centers, interpolated to the corresponding faces, and renormalized before entering the UWCDI compressive flux.

The second variant retains the sharp initialization but evaluates the normal from a locally smoothed phase field. Specifically, the symmetric nine-point filter

$$\phi^s_{i,j} = \frac{1}{16}\Big[4\phi_{i,j} + 2\left(\phi_{i+1,j} + \phi_{i-1,j} + \phi_{i,j+1} + \phi_{i,j-1}\right) + \sum_{p=\pm1}\sum_{q=\pm1}\phi_{i+p,j+q}\Big]. \tag{33}$$

is first applied to ϕ. The interface normal is then obtained from centered differences of ϕ^s, using the same subsequent cell-center normalization, face interpolation, and face renormalization as in the baseline implementation.

The third variant retains the Youngs reconstruction but replaces the sharp indicator by a diffuse hyperbolic-tangent profile,

$$\phi(\mathbf{x}, 0) = \frac{1}{2}\left[1 - \tanh\left(\frac{d(\mathbf{x})}{h}\right)\right], \qquad d(\mathbf{x}) = |\mathbf{x} - \mathbf{x}_{c,0}| - R_0, \tag{34}$$

where $h = 1/N$, $R_0 = 0.2$, and $\mathbf{x}_{c,0} = (0.6, 0.5)$. This profile has a transition width comparable to the approximately two-cell interface subsequently maintained by UWCDI.

The filtered-normal and diffuse-initialization variants test whether smoothing the phase field used to construct the normal or changing the initial profile further alters the contour.

Figure 5 compares the baseline and auxiliary configurations at $N = 128$ and $t = 2.34$, 5.86, and 8.20. Differences are most apparent during the large-deformation stages. Relative to baseline, the Youngs-type normal attenuates the strongest grid-scale corrugations, and the nine-point-smoothed normal produces a contour similar to the Youngs reconstruction. Diffuse initialization modifies the contour only modestly and does not eliminate the residual modulation. These results indicate that the local UWCDI morphology is sensitive to normal reconstruction, while the residual features cannot be attributed solely to the sharp initial profile.

The centroid trajectories remain close to the baseline throughout the simulation: the maximum separations are 9.2×10^{-4} for the Youngs reconstruction, 6.2×10^{-4} for the filtered normal, and 1.63×10^{-3} for Youngs reconstruction with diffuse initialization, relative to the unit cavity width. Across the auxiliary runs, the maximum relative phase-integral error is below 4.1×10^{-13}, and the effective interface thickness at $t = 20$ ranges from $2.00h$ to $2.02h$.

The standard centered-gradient normal is retained in the main $N = 64, 128, 256$ grid-refinement study; the auxiliary runs document sensitivity to these implementation choices.

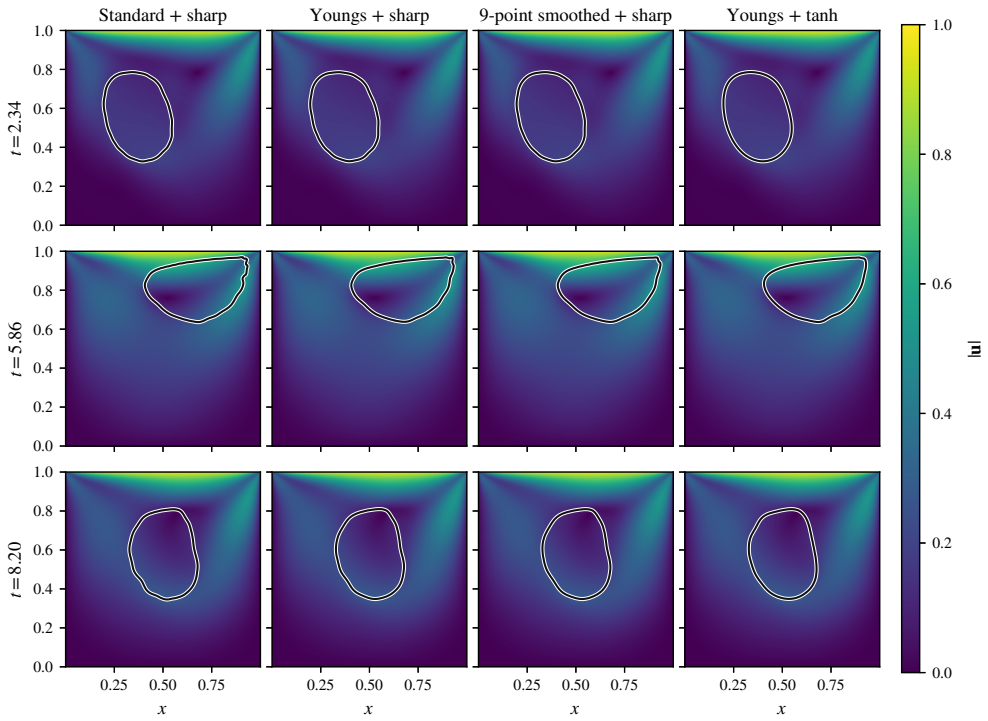


Fig. 5 Sensitivity of the UWCDI interface geometry at $N = 128$. Columns show the standard centered-gradient normal, the Youngs normal, the nine-point-smoothed normal (all with sharp initialization), and the Youngs normal with hyperbolic-tangent initialization. Rows correspond to $t = 2.34$, 5.86, and 8.20. The background denotes velocity magnitude and the overlaid contour denotes $\phi = 0.5$; all panels share the same velocity scale.

Acknowledgements. The authors gratefully acknowledge support from the FI-STEP scholarship (2025 STEP 00540) and the Serra Húnter program of the Generalitat de Catalunya (Spain). The authors are grateful to Sergio Pirozzoli and Simone Di Giorgio for insightful discussions about the UWCDI phase-field method.

Statements and Declarations

Funding. This work was funded by the Agencia Estatal de Investigación (AEI, Spain) under the BREATHE project (Grant CNS2024-154759).

Competing interests. The authors have no competing interests.

Data availability. All data supporting the findings of this study are available within the paper.

Code availability. The Julia source code and simulation configurations used in this study are publicly available at https://github.com/UPC-LCPBIO/EulerianFSI.

Author contributions. N.T.: conceptualization, data curation, formal analysis, investigation, methodology, software, validation, visualization, writing—original draft;

A.B.: conceptualization, methodology, software, writing—review and editing; S.M.M.: conceptualization, formal analysis, writing—review and editing; F.C.: conceptualization, formal analysis, funding acquisition, investigation, project administration, supervision, writing—review and editing.

References

Cavaglieri, D., Bewley, T.R.: Low-storage implicit/explicit runge–kutta schemes for the simulation of stiff high-dimensional ode systems. Journal of Computational Physics **286**, 172–193 (2015) https://doi.org/10.1016/j.jcp.2015.01.031

Chiu, P.-H., Lin, Y.-T.: A conservative phase field method for solving incompressible two-phase flows. Journal of Computational Physics **230**(1), 185–204 (2011) https://doi.org/10.1016/j.jcp.2010.09.021

Cottet, G.-H., Maitre, E., Milcent, T.: Eulerian formulation and level set models for incompressible fluid–structure interaction. ESAIM: Mathematical Modelling and Numerical Analysis **42**(3), 471–492 (2008) https://doi.org/10.1051/m2an:2008013

Drescher, K., Shen, Y., Bassler, B.L., Stone, H.A.: Biofilm streamers cause catastrophic disruption of flow with consequences for environmental and medical systems. Proceedings of the National Academy of Sciences **110**, 4345–4350 (2013) https://doi.org/10.1073/pnas.1300321110

Dunne, T.: An Eulerian approach to fluid–structure interaction and goal-oriented mesh adaptation. International Journal for Numerical Methods in Fluids **51**, 1017–1039 (2006) https://doi.org/10.1002/fld.1205

Griffith, B.E., Patankar, N.A.: Immersed methods for fluid–structure interaction. Annual Review of Fluid Mechanics **52**, 421–448 (2020) https://doi.org/10.1146/annurev-fluid-010719-060228

Hu, H.H., Patankar, N.A., Zhu, M.Y.: Direct numerical simulations of fluid–solid systems using the arbitrary Lagrangian–Eulerian technique. Journal of Computational Physics **169**, 427–462 (2001) https://doi.org/10.1006/jcph.2000.6592

Harlow, F.H., Welch, J.E.: Numerical calculation of time-dependent viscous incompressible flow of fluid with free surface. The Physics of Fluids **8**(12), 2182–2189 (1965) https://doi.org/10.1063/1.1761178

Ii, S., Gong, X., Sugiyama, K., Wu, J., Huang, H., Takagi, S.: A full Eulerian fluid–membrane coupling method with a smoothed volume-of-fluid approach. Communications in Computational Physics **12**(2), 544–576 (2012) https://doi.org/10.4208/cicp.141210.110811s

Ii, S., Sugiyama, K., Takeuchi, S., Takagi, S., Matsumoto, Y.: An implicit full Eulerian method for the fluid–structure interaction problem. International Journal for

Numerical Methods in Fluids (2011) https://doi.org/10.1002/fld.2460

Jain, S.S.: Accurate conservative phase-field method for simulation of two-phase flows. Journal of Computational Physics **469**, 111529 (2022) https://doi.org/10.1016/j.jcp.2022.111529

Jain, S.S., Kamrin, K., Mani, A.: A conservative and non-dissipative Eulerian formulation for the simulation of soft solids in fluids. Journal of Computational Physics **399**, 108922 (2019) https://doi.org/10.1016/j.jcp.2019.108922

Jemison, M., Sussman, M., Shashkov, M.: Filament capturing with the multimaterial moment-of-fluid method. Journal of Computational Physics **285**, 149–172 (2015) https://doi.org/10.1016/j.jcp.2015.01.014

Kanchan, M., Maniyeri, R.: Numerical simulation of buckling and asymmetric behavior of flexible filament using temporal second-order immersed boundary method. International Journal of Numerical Methods for Heat & Fluid Flow **30**(3), 1047–1095 (2020) https://doi.org/10.1108/HFF-06-2019-0467

Mokbel, D., Abels, H., Aland, S.: A phase-field model for fluid–structure interaction. Journal of Computational Physics **372**, 823–840 (2018) https://doi.org/10.1016/j.jcp.2018.06.063

Mittal, R., Iaccarino, G.: Immersed boundary methods. Annual Review of Fluid Mechanics **37**, 239–261 (2005) https://doi.org/10.1146/annurev.fluid.37.061903.175743

Mirjalili, S., Ivey, C.B., Mani, A.: A conservative diffuse interface method for two-phase flows with provable boundedness properties. Journal of Computational Physics **401**, 109006 (2020) https://doi.org/10.1016/j.jcp.2019.109006

Mao, X., Jaiman, R.: An interface and geometry preserving phase-field method for fully Eulerian fluid–structure interaction. Journal of Computational Physics **476**, 111903 (2023) https://doi.org/10.1016/j.jcp.2022.111903

Mirjalili, S., Jain, S.S., Dodd, M.S.: Interface-capturing methods for two-phase flows: An overview and recent developments. In: Annual Research Briefs 2017, pp. 117–135. Center for Turbulence Research, Stanford, CA (2017)

Olsson, E., Kreiss, G.: A conservative level set method for two phase flow. Journal of Computational Physics **210**, 225–246 (2005) https://doi.org/10.1016/j.jcp.2005.04.007

Pirozzoli, S., Di Giorgio, S., Rossi, D.: Efficient implementation of the Allen–Cahn phase-field method for material interface tracking. Computers & Fluids **301**, 106768 (2025) https://doi.org/10.1016/j.compfluid.2025.106768

Perot, J.B.: An analysis of the fractional step method. Journal of Computational Physics **108**(1), 51–58 (1993) https://doi.org/10.1006/jcph.1993.1162

Rosti, M.E., Brandt, L.: Numerical simulation of turbulent channel flow over a viscous hyper-elastic wall. Journal of Fluid Mechanics **830**, 708–735 (2017) https://doi.org/10.1017/jfm.2017.617

Richter, T.: A fully Eulerian formulation for fluid–structure-interaction problems. Journal of Computational Physics **233**, 227–240 (2013) https://doi.org/10.1016/j.jcp.2012.08.047

Rusconi, R., Lecuyer, S., Guglielmini, L., Stone, H.A.: Laminar flow around corners triggers the formation of biofilm streamers. Journal of the Royal Society Interface **7**, 1293–1299 (2010) https://doi.org/10.1098/rsif.2010.0096

Rycroft, C.H., Wu, C.-H., Yu, Y., Kamrin, K.: Reference map technique for incompressible fluid–structure interaction. Journal of Fluid Mechanics **898**, 9 (2020) https://doi.org/10.1017/jfm.2020.353

Sugiyama, K., Ii, S., Takeuchi, S., Takagi, S., Matsumoto, Y.: A full eulerian finite difference approach for solving fluid–structure coupling problems. Journal of Computational Physics **230**, 596–627 (2011) https://doi.org/10.1016/j.jcp.2010.09.032

Sun, P., Xu, J., Zhang, L.: Full Eulerian finite element method of a phase field model for fluid–structure interaction problem. Computers & Fluids **90**, 1–8 (2014)

Tierra, G., Pavissich, J.P., Nerenberg, R., Xu, Z., Alber, M.S.: Multicomponent model of deformation and detachment of a biofilm under fluid flow. Journal of the Royal Society Interface **12**(106), 20150045 (2015) https://doi.org/10.1098/rsif.2015.0045

Takagi, S., Sugiyama, K., Ii, S., Matsumoto, Y.: A review of full Eulerian methods for fluid structure interaction problems. Journal of Applied Mechanics **79**, 010911 (2012) https://doi.org/10.1115/1.4005184

Tryggvason, G., Scardovelli, R., Zaleski, S.: Direct Numerical Simulations of Gas–Liquid Multiphase Flows. Cambridge University Press, Cambridge (2011). https://doi.org/10.1017/CBO9780511975264

Valkov, B., Rycroft, C.H., Kamrin, K.: Eulerian method for multiphase interactions of soft solid bodies in fluids. Journal of Applied Mechanics **82**(4), 041011 (2015) https://doi.org/10.1115/1.4029765

Wick, T.: Fully Eulerian fluid–structure interaction for time-dependent problems. Computer Methods in Applied Mechanics and Engineering **255**, 14–26 (2013) https://doi.org/10.1016/j.cma.2012.11.009

Youngs, D.L.: Time-dependent multi-material flow with large fluid distortion. In: Morton, K.W., Baines, M.J. (eds.) Numerical Methods for Fluid Dynamics, pp. 273–285. Academic Press, London (1982)

Zhao, H., Freund, J.B., Moser, R.D.: A fixed-mesh method for incompressible flow–structure systems with finite solid deformations. Journal of Computational Physics **227**(6), 3114–3140 (2008) https://doi.org/10.1016/j.jcp.2007.11.019